

## Research Article

# A Reactance Compensated Three-Device Doherty Power Amplifier for Bandwidth and Back-Off Range Extension

Shichang Chen,<sup>1,2</sup> Weiwei Wang,<sup>1</sup> Kuiwen Xu,<sup>1</sup> and Gaofeng Wang<sup>1</sup> 

<sup>1</sup>The Key Lab of RF Circuits and Systems of the Ministry of Education of China, Microelectronic CAD Center, Hangzhou Dianzi University, Zhejiang, China

<sup>2</sup>State Key Laboratory of Millimeter Waves, Southeast University, Nanjing, China

Correspondence should be addressed to Gaofeng Wang; [gaofeng@hdu.edu.cn](mailto:gaofeng@hdu.edu.cn)

Received 22 October 2017; Revised 9 March 2018; Accepted 29 March 2018; Published 8 May 2018

Academic Editor: Daniele Pinchera

Copyright © 2018 Shichang Chen et al. This is an open access article distributed under the Creative Commons Attribution License, which permits unrestricted use, distribution, and reproduction in any medium, provided the original work is properly cited.

This paper proposes a new broadband Doherty power amplifier topology with extended back-off range. A shunted  $\lambda/4$  short line or  $\lambda/2$  open line working as compensating reactance is introduced to the conventional load modulation network, which greatly improves its bandwidth. Underlying bandwidth extension mechanism of the proposed configuration is comprehensively analyzed. A three-device Doherty power amplifier is implemented for demonstration based on Cree's 10 W HEMTs. Measurements show that at least 41% drain efficiency is maintained from 2.0 GHz to 2.6 GHz at 8 dB back-off range. In the same operating band, saturation power is larger than 43.6 dBm and drain efficiency is higher than 53%.

## 1. Introduction

As known to all, frequencies are scarce resources nowadays due to the booming of diverse wireless techniques. Therefore, sophisticated modulation schemes must be applied to achieve high data rates in a limited frequency bandwidth. At the same time of enjoying high data throughput, the large peak-to-average power ratios (PAPRs) accompanying these modulations also bring up several undesired effects to hardware implementations. The most evident impact is for power amplifiers (PAs), as they have to operate at large back-off regions to keep good linearity. The by-product of this feature is drastically deteriorated efficiency.

In the past few years, sorts of efficiency-boosting PA solutions such as envelop tracking [1], outphasing [2], and Doherty [3–18] have been reported to fight against efficiency reduction caused by high PAPR signals. Among them, the Doherty PA is considered as one of the best candidates, because it is simple in structure and easy for implementation. Consisting of two amplifiers (carrier and peaking) biased independently, a classical Doherty PA achieves peak efficiencies at both saturation and 6 dB back-off power conditions. This architecture has become the mainstream for base-station

PA designs. Nevertheless, certain communication schemes such as LTE-Advance and upcoming 5G may have several subcarriers; the corresponding PAPR value is still increasing. As a result, techniques like asymmetric subamplifier size [11] and multiway [14–16] for improving back-off range for Doherty PAs have been widely investigated. Large device size for the peaking PA is used in the asymmetric solution. However, it is not easy to find matched devices in practice and the acquirable range improvement is limited. The multiway structure basically brings in several peaking amplifiers and one carrier PA, which is believed to have a large back-off range, whose peak efficiency locations are defined by the number and size of the peaking amplifiers.

Besides, wideband communication is highly demanded today in order to support multiple-band and multifunction operation in a single system. Thereafter, bandwidth enhancement techniques for Doherty PA become hot research topic. In the literature, some efforts on modifying the load modulation networks (LMN) have achieved substantial improvements. However, most of them are still complicated in structures and are mainly limited to conventional two-way Doherty architecture [7–13].

Based on the authors' previous work presented in [18], two novel LMN configurations with shunt compensating reactance are proposed in this paper. By introducing  $\lambda/4$  short line or  $\lambda/2$  open line to the conventional LMN, the modulated impedance can have greatly reduced variation against frequency deviation, therefore improving the overall bandwidth of the Doherty PA. Systematical design concept and comprehensive theoretical analysis of the two new structures are given for good illustration.

The remainder of this paper is organized as follows. Section 2 explains the underlying confinement of the conventional structure and introduces the principle of the proposed designs. In Section 3, a three-device Doherty PA circuit with large high-efficiency back-off range is realized for demonstration. Simulated and measured results are also presented, and decent wideband operational characteristics are successfully obtained. Finally, Section 4 gives the conclusion.

## 2. Proposed Load Modulation Network

**2.1. Background.** As the key element of a Doherty PA, the conventional LMN is made up of two impedance inverters.  $\lambda/4$  transmission lines are generally adopted as a common practice. However, due to the frequency dispersion effect of the  $\lambda/4$  transformers, the conventional LMN is inherently narrow in bandwidth, which finally confines the bandwidth of the entire Doherty PA. In other words, proper load modulation can be maintained only at a single frequency. When the operational frequency deviates from the center ( $f_0$ ), the impedance modulated reduces quickly from the nominal value and PA's efficiency deteriorates as a consequence [6, 7]. Fortunately, it is found that the impedance bandwidth of the LMN can be increased by properly adding a reactive element to neutralize this dispersion. In [6], a LC shunt network is exploited as compensating reactance. However, detailed operational mechanism analysis is not given, and the highest frequency that can support is limited due to the low  $Q$ -factor of the LC resonant circuit.

Two novel LMN topologies with shunt stubs are proposed herein to have extended operational bandwidth. A shunt  $\lambda/4$  short stub and  $\lambda/2$  open stub are connected to the junction point of the subamplifiers, as shown in Figures 1(b) and 1(c), respectively. Detailed analysis will be given to verify the potentiality of the proposed ideas. Based on this, a three-device design with large bandwidth and back-off range is then implemented for verification.

**2.2. Proposed LMN with a Shunt Quarter-Wavelength Short Stub.** As well known, the operation of a Doherty PA is roughly classified into two conditions: low-power and high-power. When the power is low, the carrier amplifier operates only and it completely determines the overall performance.

Define the center frequency as  $f_0$  and the normalized frequency as  $\bar{f} = f/f_0$ . For the typical LMN as shown in Figure 1(a), the impedance seen at the junction point  $Z_{J,\text{conv}}$  is frequency dependent, and its expression is calculated as below according to classic transmission line theory [19]

$$Z_{J,\text{conv}} = Z_L \frac{Z_0 + jZ_L \tan(\bar{f} \cdot \pi/2)}{Z_L + jZ_0 \tan(\bar{f} \cdot \pi/2)}, \quad (1)$$

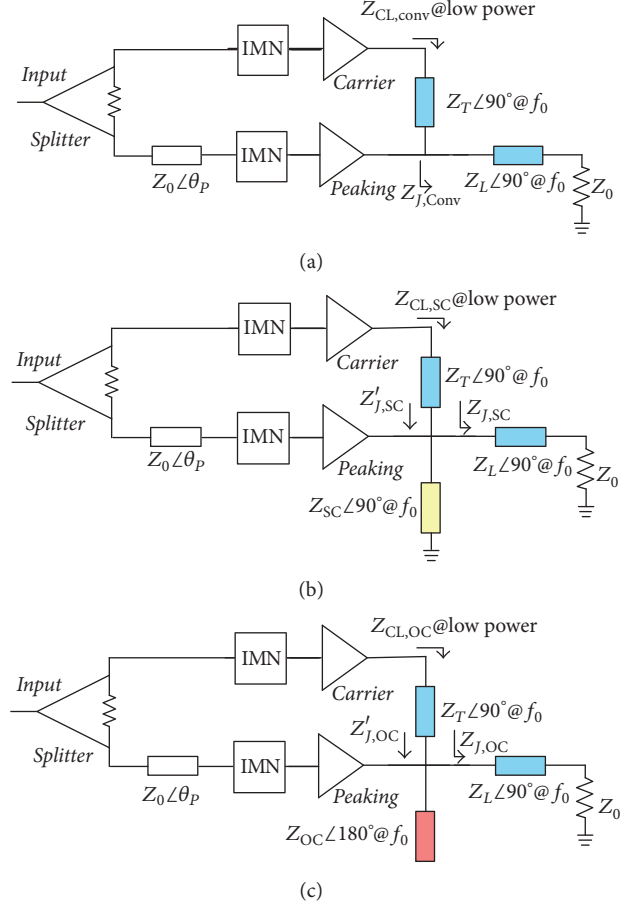


FIGURE 1: Simplified Doherty PA diagrams based on (a) conventional LMN; (b) LMN with  $\lambda/4$  short stub; (c) LMN with  $\lambda/2$  open stub.

where  $Z_L$  is the characteristic impedance of the output  $\lambda/4$  line and  $Z_0$  stands for the load ( $50 \Omega$  typically).

As a consequence, the carrier PA impedance produced by the conventional LMN  $Z_{CL,\text{conv}}$  can be expressed as

$$Z_{CL,\text{conv}} = Z_T \frac{Z_{J,\text{conv}} + jZ_T \tan(\bar{f} \cdot \pi/2)}{Z_T + jZ_{J,\text{conv}} \tan(\bar{f} \cdot \pi/2)}, \quad (2)$$

where  $Z_T$  represents the characteristic impedance of the  $\lambda/4$  line after the carrier PA.

On the other hand, for the proposed LMN shunted with  $\lambda/4$  short line as shown in Figure 1(b), the expression of the impedance for the carrier  $Z_{CL,\text{SC}}$  is now derived using the following equations:

$$Y_{J,\text{SC}} = \frac{1}{Z_{J,\text{SC}}} = \frac{1}{Z_L} \frac{Z_L + jZ_0 \tan(\bar{f} \cdot \pi/2)}{Z_0 + jZ_L \tan(\bar{f} \cdot \pi/2)}, \quad (3)$$

$$Z'_{J,\text{SC}} = \frac{1}{(Y_{J,\text{SC}} - j/Z_{SC} \tan(\bar{f} \cdot \pi/2))}, \quad (4)$$

$$Z_{CL,SC} = Z_T \frac{Z'_{J,SC} + jZ_T \tan(\bar{f} \cdot \pi/2)}{Z_T + jZ'_{J,SC} \tan(\bar{f} \cdot \pi/2)}, \quad (5)$$

where the subscript SC denotes short circuit condition and  $Z_{SC}$  is the characteristic impedance of the shunt line. Based on (2) and (5), the real and imaginary parts of the carrier impedance against frequency can be extracted by simple mathematical derivations.

Figure 2 depicts the frequency response of  $Z_{CL,SC}$  under different  $Z_{SC}$  values (12, 17, and 22 Ohms) along with that of  $Z_{CL,conv}$ . It needs to stress that the normalized values (to  $Z_0$ ) of  $Z_T$  and  $Z_L$  are unity and  $1/\sqrt{2}$  in this particular comparison, same as the classical Doherty LMN treatment. As can be observed from the figure, in each single case the carrier impedances produced by both cases are maintained around  $100 \Omega$  ( $2Z_0$ ) at the center frequency, agreeing with the classical Doherty PA theory. This is because  $\lambda/4$  short line produces infinite impedance at the center frequency, which has no influence on the modulated impedance. Nevertheless, when the operation frequency deviates from  $f_0$ , the real part of the carrier impedance produced by the conventional LMN decreases sharply. This impedance reduction usually translates to unwanted efficiency degradation and bandwidth reduction. In contrast, by adding the shunt line as compensating reactance, much more stabilized impedances are achieved in a certain band by applying the proposed topological scheme, as indicated by the larger and flatter real part response.

For the imaginary side, all cases exhibit similar capacitive/inductive behaviors at frequencies above/below the center frequency. However, the variation presented by the conventional LMN is much larger than that of the proposed LMNs. From the PA design aspect, a much flatter ohmic and smaller

reactive loading usually means it is easier to design a broadband matching network and achieve larger bandwidth afterwards [7]. At the center frequency, the shunt stub is equivalent to an open-circuit load seen at the junction point; therefore no loading effect occurs. This is demonstrated by the identical load impedances presented at  $f_0$  for all the configurations analyzed.

In the high-power condition, all subamplifiers operate. Suppose the fundamental currents produced by the two sub-amplifier cells are identical, the corresponding impedances can be easily calculated based on the diagram shown in Figures 1(a) and 1(b). Figures 3 and 4 compare the simulated carrier and peaking impedance behaviors at saturation with different LMN schemes, whose real and imaginary parts are monitored separately. It is obvious that the carrier impedance has similar profile to that of the low-power condition. To be specific, impedance variations against frequency deviation are significantly suppressed, for both the imaginary and real parts. On the peaking side, although the conventional design shows relative flatter impedance responses, the variation ratio is not as much as that for the carrier PA. Thus, by optimizing the characteristic impedances of the shunt stub, overall bandwidth enhancement can still be ensured.

### 2.3. Proposed LMN with a Shunt Half-Wavelength Open Stub.

Similar to the configuration shown above, a shunt  $\lambda/2$  open stub can also be used as effective compensating reactance. The theoretical analysis of the configured LMN with a shunt  $\lambda/2$  open stub is much alike to the aforementioned case. Figure 1(c) gives its schematic diagram. The carrier impedance at the low-power condition  $Z_{CL,OC}$  can be derived as

$$Z'_{J,OC} = \frac{1}{\left( \frac{1}{Z_L} \left( (Z_L + jZ_0 \tan(\bar{f} \cdot \pi/2)) / (Z_0 + jZ_L \tan(\bar{f} \cdot \pi/2)) \right) + j \tan(\bar{f} \cdot \pi/2) / Z_{OC} \right)}, \quad (6)$$

$$Z_{CL,OC} = Z_T \frac{Z'_{J,OC} + jZ_T \tan(\bar{f} \cdot \pi/2)}{Z_T + jZ'_{J,OC} \tan(\bar{f} \cdot \pi/2)},$$

where  $Z_{OC}$  is the characteristic impedance of the shunt line and the subscript OC denotes open circuit.

Figure 5 compares the calculated  $Z_{CL,OC}$  behaviors of different  $Z_{OC}$  values (24, 44, and 64 Ohms) along with that of  $Z_{CL,conv}$ . The normalized impedances  $Z_T$  and  $Z_L$  are again unity and  $1/\sqrt{2}$ . It can be seen that, by adopting a proper characteristic impedance (e.g., 44  $\Omega$ ), the modulated impedances from the proposed LMN may have a much flatter response versus frequency than that the conventional LMN can provide. Curves for impedances presented to the carrier and peaking subamplifiers at high-power condition are shown in Figures 6 and 7, respectively. As before, once the characteristic impedance of the shunt stub is appropriately chosen, smaller variation of the carrier impedance is achievable for the proposed topology by contrast with the conventional design. As a consequence, larger bandwidth can

be obtained as impedance matching becomes much easier. In addition, the two compensating methods mentioned above generally have different parameters regarding characteristic impedance and length. In practice, which configuration to use is mainly decided after considering the bandwidth effects and realization convenience overall.

## 3. Circuit Realization

### 3.1. Wideband Three-Device Doherty Power Amplifier Design.

To deal with signals with high PAPRs, total peaking device periphery must be larger than that of the carrier device. Herein, a dual-peaking single-carrier Doherty PA is therefore devised, aiming at large back-off range. In order to have wideband operational capability at the same time, the LMN

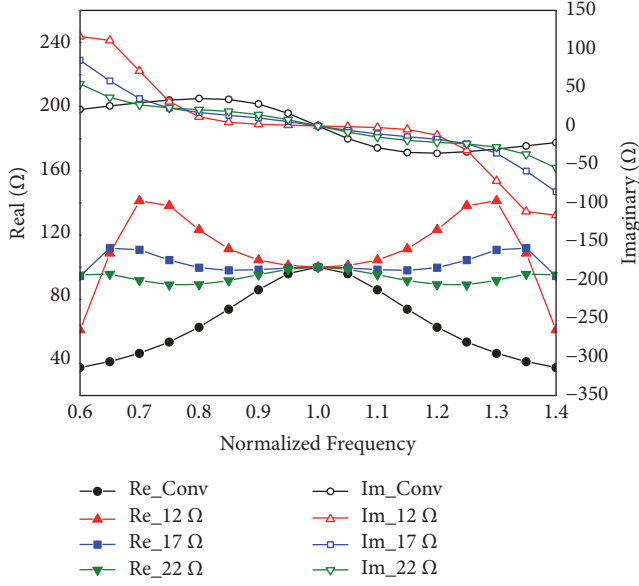


FIGURE 2: Carrier impedance comparison between the conventional LMN and the wideband LMN with a shunt  $\lambda/4$  short stub of different characteristic impedances at low-power condition.

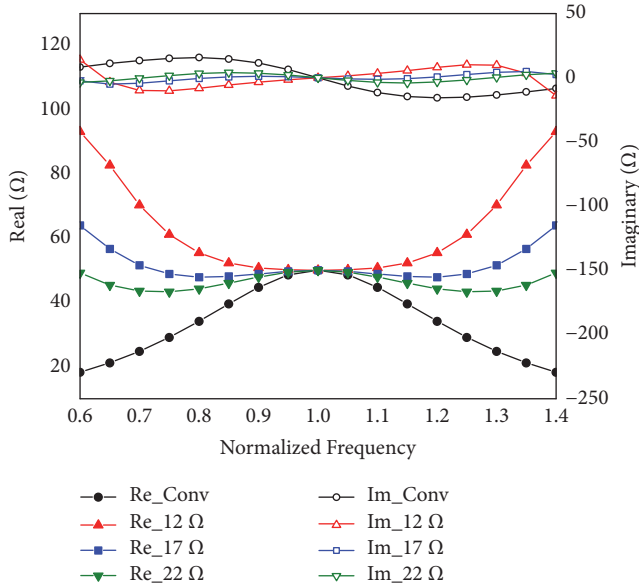


FIGURE 3: Carrier impedance comparison between the conventional LMN and the wideband LMN with a shunt  $\lambda/4$  short stub of different characteristic impedances at high-power condition.

with a shunted short  $\lambda/4$  stub analyzed above is updated to fit a three-way structure, as depicted in Figure 8. Specifically speaking, the carrier PA is placed at the center, whose output is evenly shared by the two symmetrically aligned peaking amplifiers to form load modulation.

It is well acknowledged that the operation of a Doherty PA differs at low-power and high-power regions. For low-power scenario, both peaking PAs are turned off and the carrier PA operates solely. The shunt  $\lambda/4$  line on each branch

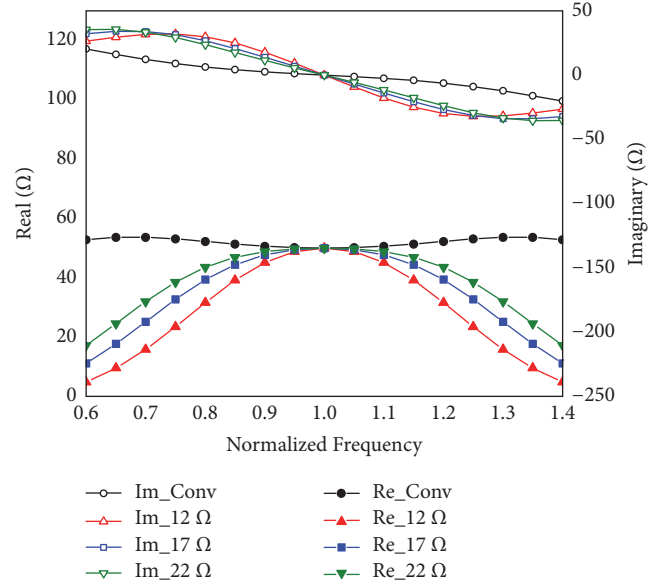


FIGURE 4: Peaking impedances at high-power condition for the conventional LMN and the proposed LMN with a shunt  $\lambda/4$  short stub of different characteristic impedances.

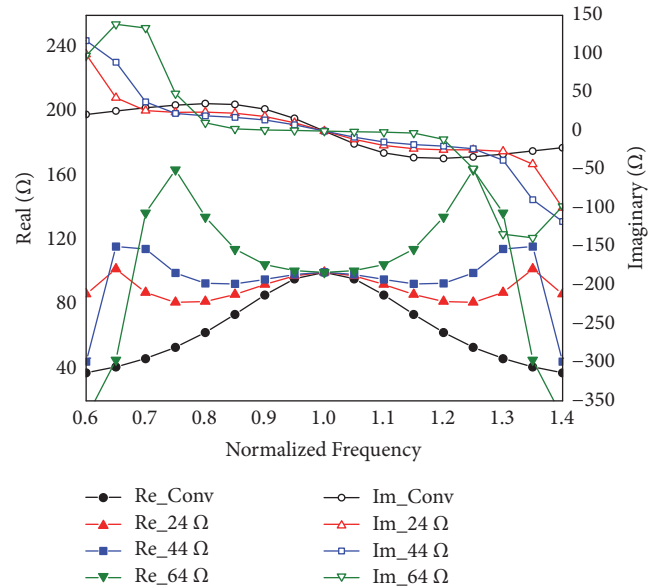


FIGURE 5: Carrier impedance comparison between the conventional LMN and the wideband LMN with a shunt  $\lambda/2$  open stub of different characteristic impedances at low-power condition.

is divided into two parts at the junction  $VP_i$  ( $i = 1, 2$ ). As long as each peaking PA is connected with a proper offset line after the output matching network, the impedances seen into the peaking PAs from the two junction points  $VP_1$  and  $VP_2$  can be made very high [5]. Reverse power leakage is therefore prevented. In other words, the peaking branches are *isolated* from the shunt line, and this LMN is degenerated to that of the shunt stub configuration introduced before for the carrier PA. The impedance presented exhibits frequency response similar

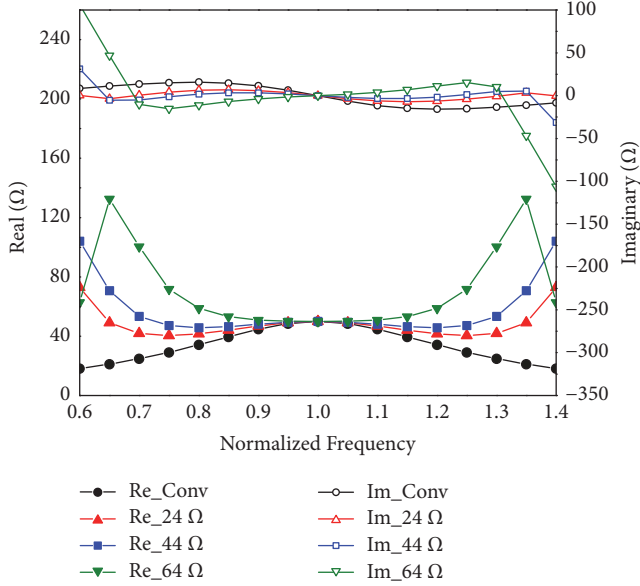


FIGURE 6: Carrier impedance comparison between the conventional LMN and the wideband LMN with a shunt  $\lambda/2$  open stub of different characteristic impedances at high-power condition.

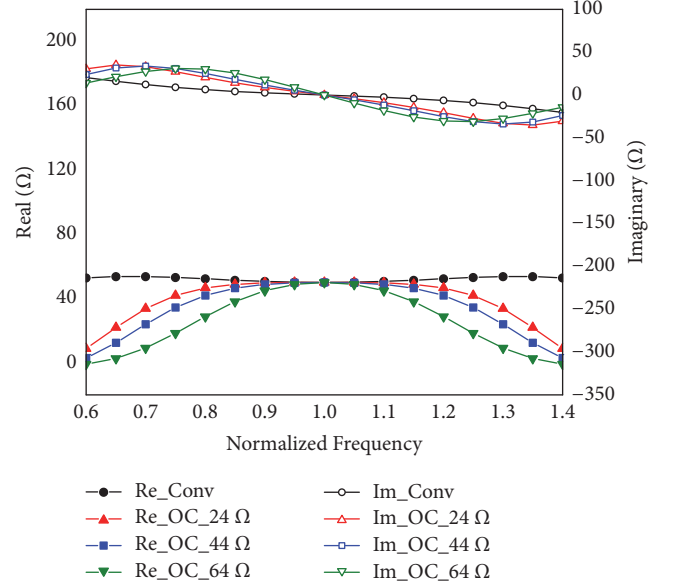


FIGURE 7: Peaking impedances for the conventional LMN and the proposed LMN with a shunt  $\lambda/2$  open stub of different characteristic impedances at high-power condition.

to that shown in Figure 2. That is to say, when input is low, the carrier PA operates only, and its impedance  $Z_{CL,prop}$  can be calculated as

$$\begin{aligned}
 Y_{J,prop} &= \frac{1}{Z_{J,prop}} = \frac{1}{Z_L Z_0 + jZ_L \tan(\bar{f} \cdot \pi/2)}, \\
 Z'_{J,prop} &= \frac{1}{(Y_{J,prop} - 2(j/Z_{SC} \tan(\bar{f} \cdot \pi/2)))}, \\
 Z_{CL,prop} &= Z_T \frac{Z'_{J,prop} + jZ_T \tan(\bar{f} \cdot \pi/2)}{Z_T + jZ'_{J,prop} \tan(\bar{f} \cdot \pi/2)},
 \end{aligned} \quad (7)$$

where the subscript SC denotes the short-stub attachment as before. The characteristic impedances of the shunt lines are  $Z_{SC}$ . Figure 9 depicts the simulated  $Z_{CL,prop}$  responses against different  $Z_{SC}$  values (25, 35, and 45 Ohms). It is intuitive that if the  $Z_{SC}$  value is carefully chosen, this scenario is positive for bandwidth enhancement, as similar to the case introduced above in Section 2.2.

When input increases, the two peaking PAs conduct gradually and form active load modulation with the carrier PA. Set the fundamental saturation current ratio of the sub-amplifiers as  $\delta = I_P/I_C$ .  $I_P$  and  $I_C$  represent the saturation current for the carrier and peaking amplifiers, respectively. According to [3, 4], for optimal impedance matching, the characteristic impedances of  $Z_T$  and  $Z_L$  are chosen as

$$\begin{aligned}
 Z_T &= \delta \cdot Z_0 \\
 Z_L &= \sqrt{\frac{\delta^2}{1 + 2\delta^2}} \cdot Z_0.
 \end{aligned} \quad (8)$$

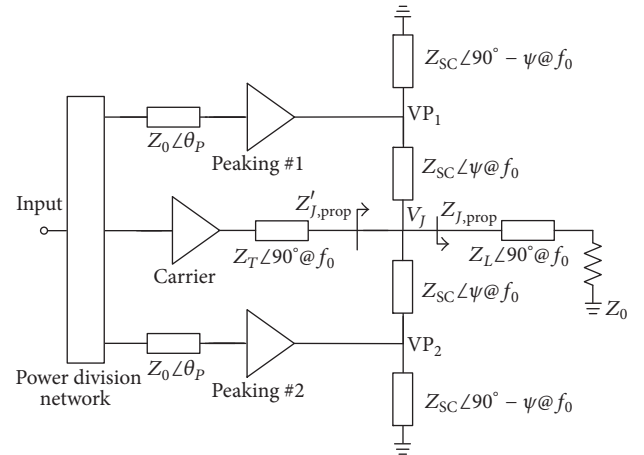


FIGURE 8: Simplified schematic of the devised Doherty PA.

In this context, the impedances presented to the carrier and two peaking amplifiers at saturation can be easily obtained once the  $Z_T$  and  $Z_L$  values are prescribed. In this particular design, what remains to mention is that the  $\psi$  value (in degrees) can be optimized, as shown in Figure 8. This offers another degree of design freedom for the output matching network. The characteristic impedance  $Z_{SC}$  is then tuned to achieve traded-off performances among the carrier and peaking subamplifiers. Figure 10 gives the simulated carrier and peaking impedance responses versus frequency at saturation for a typical case with  $\delta$  and  $Z_{SC}$  values of unity and 35  $\Omega$ , respectively. In Figure 11, the load impedance variation profiles of the subamplifiers are depicted as a function of normalized input voltage. As one can see, typical Doherty impedance profiles [3, 8] are successfully achieved.

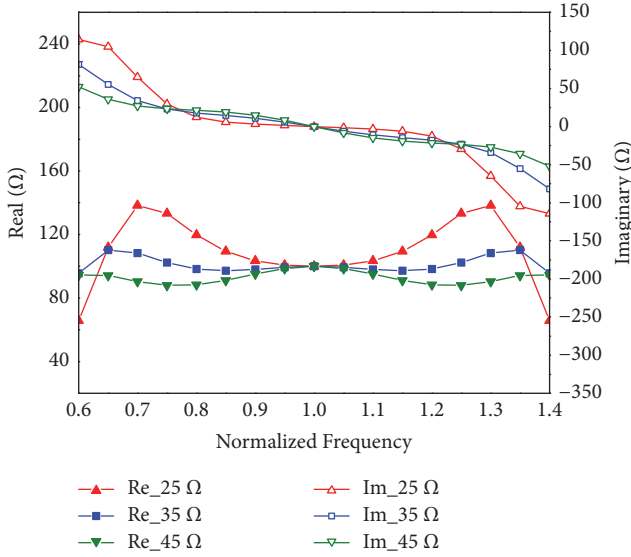


FIGURE 9: Carrier impedance of the proposed three-device DPA with shunt lines of different characteristic impedances at low-power condition.

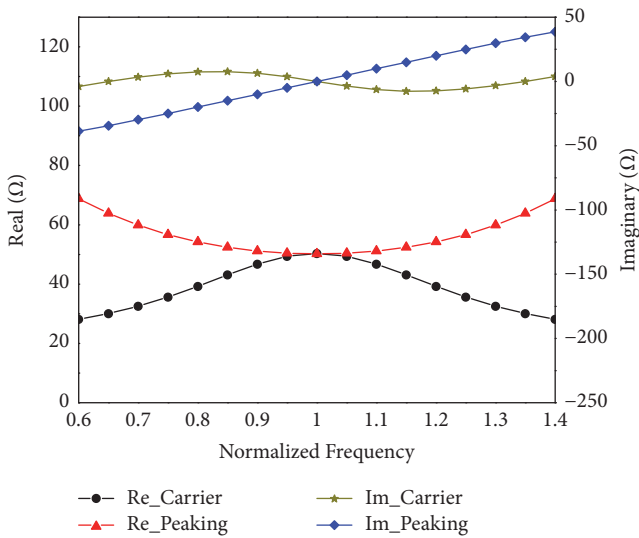


FIGURE 10: Carrier and peaking impedances for the proposed three-device DPA with  $\delta = 1$  and  $Z_{SC} = 35 \Omega$  at high-power condition.

At the input terminal, a wideband power division network is used to distribute the input power into three paths. As the same transistors are used to build the three subamplifiers, the power gain of the peaking cells is smaller than that of the carrier cell due to their lower biasing conditions. As a result, uneven power division is chosen to deliver larger power to the peaking paths. Figure 12 shows the diagram of the devised wideband power division network. Port 1 is the input terminal, and port 2 is connected to the carrier PA, whereas ports 3 and 4 are for the peaking paths. The upper and lower parts are exactly the same, and the isolation resistors  $R_1 = R_2 = 100 \Omega$ . The characteristic impedances of the six lines are  $Z_1 = 64.1 \Omega$ ,  $Z_2 = 91.7 \Omega$ ,  $Z_3 = 44.2 \Omega$ , and  $Z_4 = 57.1 \Omega$ . All the transmission lines

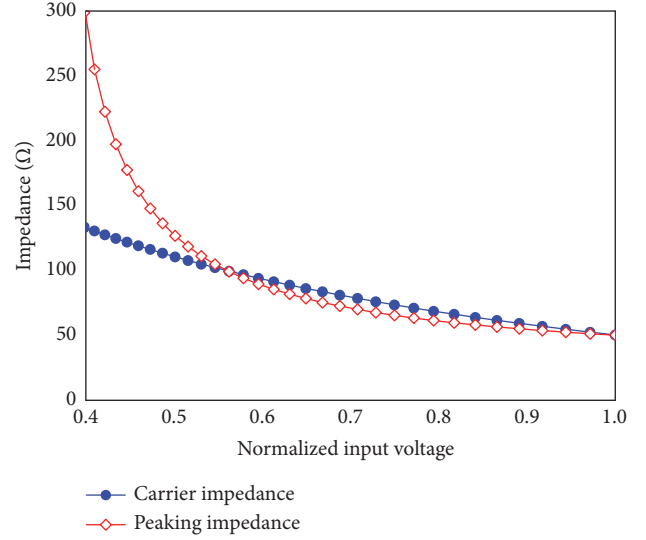


FIGURE 11: Carrier and peaking impedance variations for the proposed three-device DPA with  $\delta = 1$  and  $Z_{SC} = 35 \Omega$  as a function of input voltage.

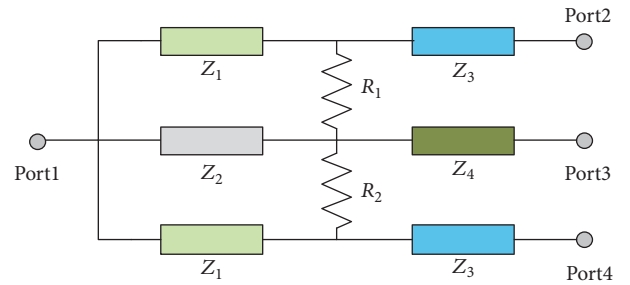


FIGURE 12: Wideband three-way uneven power divider diagram.

are  $\lambda/4$  long at the center frequency  $f_0$  ( $f_0$  equals 2.3 GHz in this particular design). Figure 13 depicts the simulated performance of the divider in Keysight ADS momentum. Note that  $S_{31}$  and  $S_{41}$  are maintained around  $-6.2$  dB and  $-4.6$  dB throughout the frequency band from 1.5 to 3.0 GHz. This means that the stimulus for peaking PAs is about 1.5 dBm larger than that for the carrier PA. This treatment is intended for identical driving capabilities at saturation among the three subamplifiers. In addition, the return losses and isolations between the output ports are all below  $-15$  dB.

As optimal source and load impedances change with operating frequency, extensive source-pull and load-pull simulations are conducted to find the frequency-dependent target impedances. Output matching networks and offset lines are carefully designed to maintain broadband operation of the whole Doherty PA. Besides, broadband input matching networks with the classical cascaded low-pass type topology are designed for all the three subamplifiers before final circuit assembly. A phase balance line is also added at the peaking input in order to maximize saturation output power. Furthermore, DC supplies can be directly added to end of the short stubs in the meantime, making DC powering more

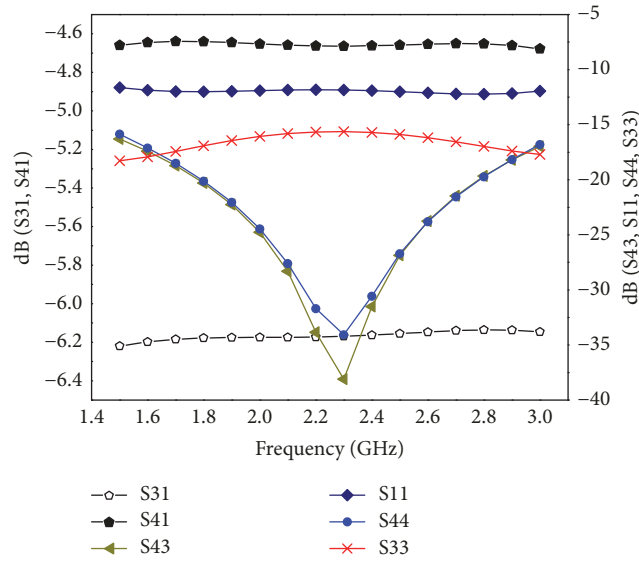


FIGURE 13: Simulated performances of the devised three-way uneven power division network.

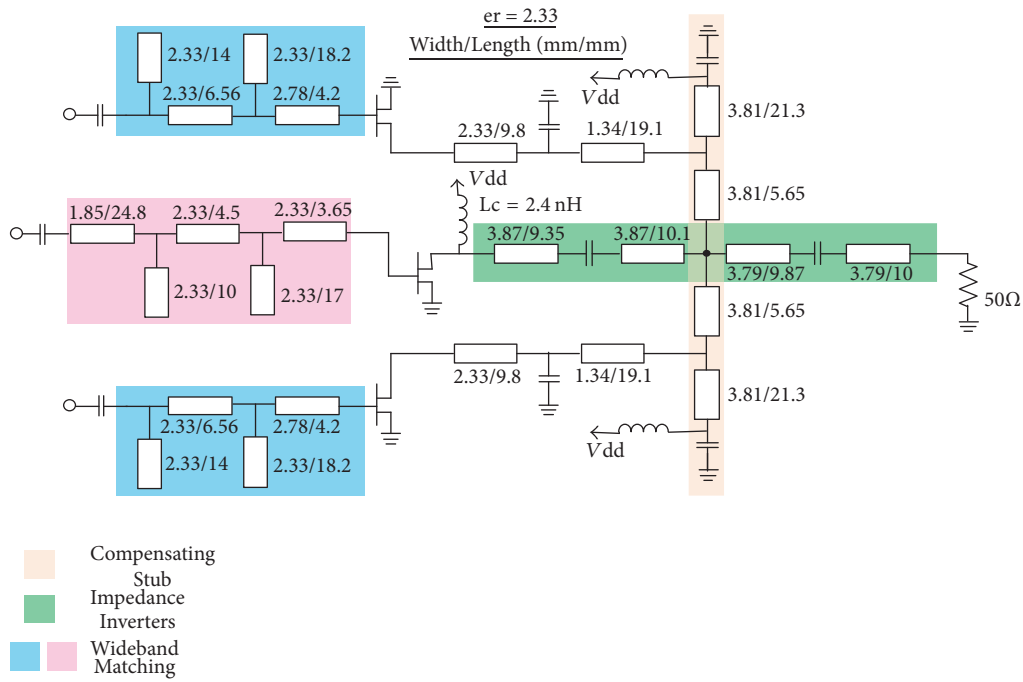


FIGURE 14: Final topology of the implemented DPA structure.

convenient. Careful optimization has been made to ensure decent performances in a large operational bandwidth.

Figure 14 gives the topology of the realized Doherty PA, shown at the bottom of this page. Input power division network is not plotted for the sake of simplicity. The prototype circuit is implemented on a Duroid 5870 substrate with permittivity of 2.33 and a height of 31 mil. The demonstrating hardware for the open stub case described in Section 2.3 is not

devised, because these two configurations have similar theoretical fundamentals for bandwidth extension as introduced above.

3.2. *Simulated and Measured Results.* This particular three-way circuit is fully characterized in Keysight ADS simulator. All subamplifiers are constructed with the 10-W GaN HEMT CGH40010 provided by Cree. Simulations are performed

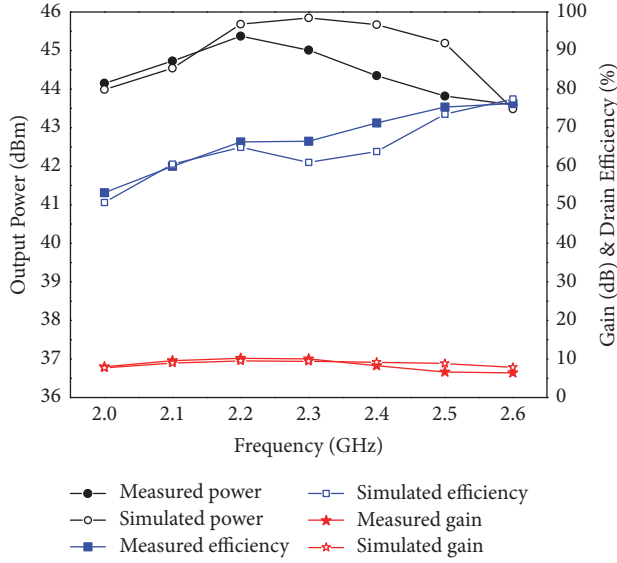


FIGURE 15: Efficiency and gain curves from simulation and measurement of the implemented prototype at saturation condition.

with a large signal transistor model provided by manufacture. Biasing conditions are carefully optimized to realize the power dependent opening sequences of the subamplifiers. To be specific, the carrier cell is biased at  $-2.7$  V, corresponding to class-AB mode. On the other hand, the biasing voltages of the two peaking cells are  $-6.5$  V, corresponding to class-C mode. The supply voltages ( $V_{dd}$ ) are all set to 28 V. By careful device alignment and wiring, the entire circuit is kept concise and symmetry.

Figure 15 shows the simulated and measured characteristics at saturation under continuous wave (CW) excitation in terms of gains, maximum output powers, and drain efficiencies of the designed Doherty PA. It is clear to see that a minimum of 53% drain efficiency is recorded in measurement in a 600 MHz bandwidth, ranging from 2.0 GHz to 2.6 GHz. 76% efficiency is obtained at 2.6 GHz, which is the highest value in this observed band. In addition, at least 43.6 dBm output power is maintained, and a peak value of 45.4 dBm appears at 2.2 GHz. The measurements and simulations agree well, and the small discrepancies may be caused by model inaccuracy, fabrication tolerance, and so on.

As two peaking amplifiers are applied, the total device periphery of the peaking part is larger than the carrier part, and thus an increased power back-off range is realized. Figure 16 compares the tested and simulated gain and drain efficiency curves at 8 dB back-off power from 2.0 GHz to 2.6 GHz. Throughout this frequency band, over 41% drain efficiency is successfully maintained. This accounts for a rational frequency bandwidth of 26%.

To better characterize the efficiency profile of the fabricated circuit, Figure 17 depicts the registered gain and drain efficiency profiles as a function of the output power in the same frequency band with a 100 MHz interval. It is readily seen that the proposed Doherty PA approximately follows the classic Doherty type efficiency profiles at all the frequency

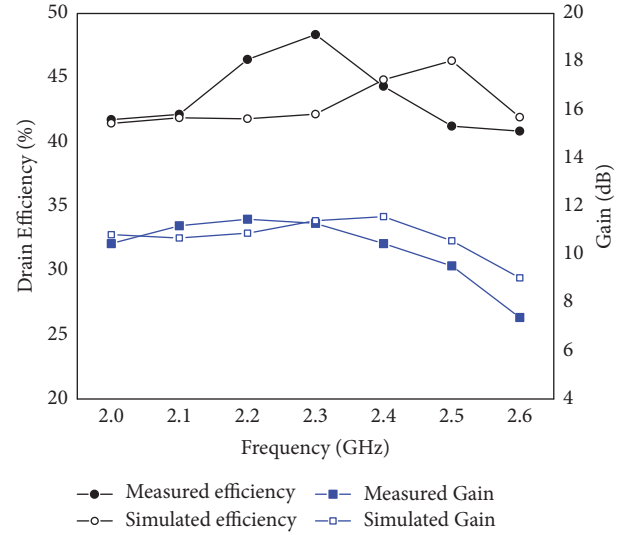


FIGURE 16: Efficiency and gain curves from simulation and measurement of the implemented prototype at 8 dB back-off range.

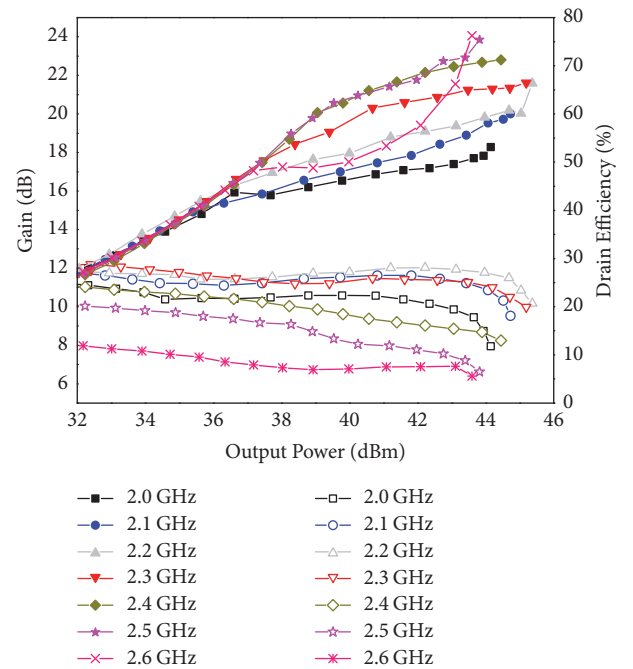


FIGURE 17: Registered gain and drain efficiency profiles as a function of output power.

components. Table 1 lists the comparison of several published wideband Doherty PAs and this work.

Moreover, a 20 MHz LTE modulated signal with 8 dB PAPR value is used to test the proposed circuit prototype for further performance evaluation. Figure 18 gives the registered average drain efficiency and adjacent channel leakage ratios (ACLR) as a function of output power at 2.3 GHz. It is readily seen that about 46% drain efficiency is achieved at 8 dB back-off power, while the corresponding ACLR value is around  $-29$  dBc. Besides, digital predistortion (DPD) technique [20]

TABLE I: Performance summary of broadband Doherty PAS.

Ref.	Config.	Freq. (GHz)	DE. @ Sat. (Max/Min%)	DE. @ OBO (Max/Min%)	Pout (dBm)
[6]	2-way	0.7–0.95	67/53	56/48 @6-dB	>43
[7]	2-way	3.0–3.6	66/55	56/38 @6-dB	43–44
[8]	2-way uneven biasing	1.7–2.6	55/50	55/41 @6-dB	42.1–45.3
[11]	2-way die	1.05–2.55	83/45	58/35 @6-dB	44.6–46.3
[12]	2-way	1.96–2.46	60/46	44/40 @6-dB	39.8–41.7
[15]	3-way	0.73–0.98	67/53	64/49 @9dB	42.7–44.6
[16]	3-stage uneven biasing	0.7–0.95	75/60	65/47 @9-dB	42.9–44.7
This work	3-device	2.0–2.6	76/53	48/41 @8-dB	43.6–45.4

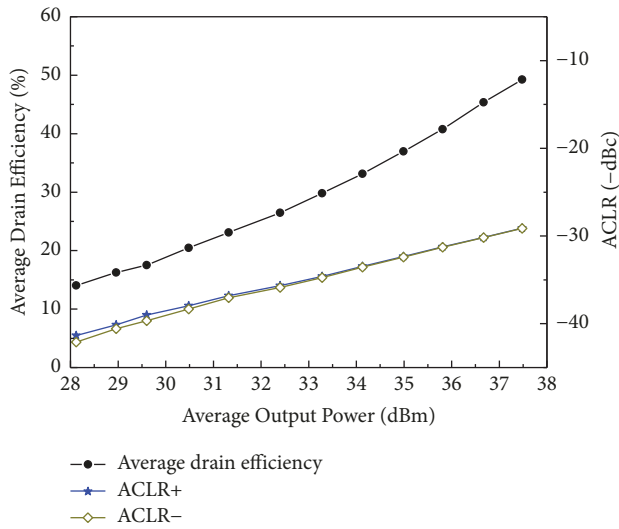


FIGURE 18: Measured average drain efficiency and ACLR values as a function of average output power at 2.3 GHz under a 20 MHz LTE signal excitation.

is applied to the devised DPA, and the ACLR value reduced to  $-51$  dBc after DPD treatment, which indicates a good linearization capability. Figure 19 depicts the photography of the fabricated Doherty PA.

#### 4. Conclusion

Two new load modulation networks with a shunt  $\lambda/4$  short stub and  $\lambda/2$  open stub to improve Doherty PA bandwidth have been proposed. Underlying principles regarding the bandwidth merits have been fully analyzed. A single-carrier dual-peaking Doherty PA circuit was implemented based on the updated topological scheme for verification. Large bandwidth and high-efficiency back-off range are achieved simultaneously.

#### Conflicts of Interest

The authors declare that they have no conflicts of interest.

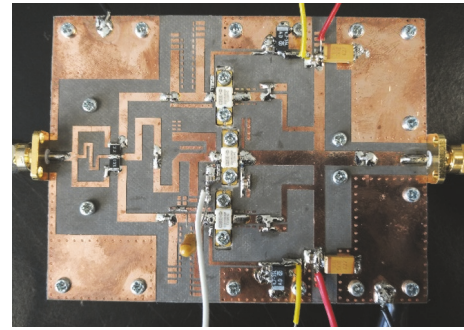


FIGURE 19: Photography of the fabricated three-device Doherty PA.

#### Acknowledgments

This work was supported in part by the National Natural Science Foundation of China under Grants no. 61601160, no. 61411136003, and no. 61331007 and by the Open Research Fund of Key Laboratory of Millimeter Waves, Southeast University, under Grant no. K201820.

#### References

- [1] S. Jin, B. Park, K. Moon et al., "A Highly Efficient CMOS Envelope Tracking Power Amplifier Using All Bias Node Controls," *IEEE Microwave and Wireless Components Letters*, vol. 25, no. 8, pp. 517–519, 2015.
- [2] S. Lee and S. Nam, "A cmos outphasing power amplifier with integrated single-ended chireix combiner," *IEEE Transactions on Circuits and Systems II: Express Briefs*, vol. 57, no. 6, pp. 411–415, 2010.
- [3] S. Chen and Q. Xue, "Optimized load modulation network for doherty power amplifier performance enhancement," *IEEE Transactions on Microwave Theory and Techniques*, vol. 60, no. 11, pp. 3474–3481, 2012.
- [4] S. Chen, Z. Cheng, G. Wang, and Q. Xue, "Compact Doherty Power Amplifier Design for  $2 \times 2$  Multiple-Input Multiple-Output System," *IEEE Microwave and Wireless Components Letters*, vol. 26, no. 3, pp. 216–218, 2016.
- [5] R. Quaglia, M. Pirola, and C. Ramella, "Offset lines in doherty power amplifiers: Analytical demonstration and design," *IEEE*

- Microwave and Wireless Components Letters*, vol. 23, no. 2, pp. 93–95, 2013.
- [6] M. N. A. Abadi, H. Golestaneh, H. Sarbishaei, and S. Boumaiza, “An extended bandwidth Doherty power amplifier using a novel output combiner,” in *Proceedings of the 2014 IEEE MTT-S International Microwave Symposium, IMS 2014*, Tampa, Fla, USA, June 2014.
  - [7] J. M. Rubio, J. Fang, V. Camarchia, R. Quaglia, M. Pirola, and G. Ghione, “3-3.6-GHz wideband GaN Doherty power amplifier exploiting output compensation stages,” *IEEE Transactions on Microwave Theory and Techniques*, vol. 60, no. 8, pp. 2543–2548, 2012.
  - [8] K. Bathich, A. Z. Markos, and G. Boeck, “Frequency response analysis and bandwidth extension of the Doherty amplifier,” *IEEE Transactions on Microwave Theory and Techniques*, vol. 59, no. 4, pp. 934–944, 2011.
  - [9] D. Gustafsson, C. M. Andersson, and C. Fager, “A modified doherty power amplifier with extended bandwidth and reconfigurable efficiency,” *IEEE Transactions on Microwave Theory and Techniques*, vol. 61, no. 1, pp. 533–542, 2013.
  - [10] R. Giofre, P. Colantonio, F. Giannini, and L. Piazzon, “New output combiner for doherty amplifiers,” *IEEE Microwave and Wireless Components Letters*, vol. 23, no. 1, pp. 31–33, 2013.
  - [11] R. Giofre, L. Piazzon, P. Colantonio, and F. Giannini, “A closed-form design technique for ultra-wideband doherty power amplifiers,” *IEEE Transactions on Microwave Theory and Techniques*, vol. 62, no. 12, pp. 3414–3424, 2014.
  - [12] M. Akbarpour, M. Helaoui, and F. M. Ghannouchi, “A transformer-less load-modulated (TLLM) architecture for efficient wideband power amplifiers,” *IEEE Transactions on Microwave Theory and Techniques*, vol. 60, no. 9, pp. 2863–2874, 2012.
  - [13] J. Qureshi, W. Sneijers, R. Keenan, L. deVreede, and F. van Rijs, “A 700-W peak ultra-wideband broadcast Doherty amplifier,” in *Proceedings of the 2014 IEEE/MTT-S International Microwave Symposium - MTT 2014*, pp. 1–4, Tampa, Fla, USA, June 2014.
  - [14] Y. Yang, J. Cha, B. Shin, and B. Kim, “A fully matched N-way Doherty amplifier with optimized linearity,” *IEEE Transactions on Microwave Theory and Techniques*, vol. 51, no. 3, pp. 986–993, 2003.
  - [15] H. Golestaneh, F. A. Malekzadeh, and S. Boumaiza, “An extended-bandwidth three-way doherty power amplifier,” *IEEE Transactions on Microwave Theory and Techniques*, vol. 61, no. 9, pp. 3318–3328, 2013.
  - [16] A. Barthwal, K. Rawat, and S. Koul, “Bandwidth Enhancement of Three-Stage Doherty Power Amplifier Using Symmetric Devices,” *IEEE Transactions on Microwave Theory and Techniques*, vol. 63, no. 8, pp. 2399–2410, 2015.
  - [17] S. Chen, G. Wang, Z. Cheng, P. Qin, and Q. Xue, “Adaptively Biased 60-GHz Doherty Power Amplifier in 65-nm CMOS,” *IEEE Microwave and Wireless Components Letters*, vol. 27, no. 3, pp. 296–298, 2017.
  - [18] S. Chen, P. Qiao, G. Wang, Z. Cheng, and Q. Xue, “A broadband three-device Doherty power amplifier based on a modified load modulation network,” in *Proceedings of the 2016 IEEE/MTT-S International Microwave Symposium (IMS)*, pp. 1–4, San Francisco, Calif, USA, May 2016.
  - [19] D. M. Pozar, *Microwave Engineering*, John Wiley & Sons, Inc, New York, NY, USA, 2nd edition, 1998.
  - [20] D. R. Morgan, Z. Ma, J. Kim, M. G. Zierdt, and J. Pastalan, “A generalized memory polynomial model for digital predistortion of RF power amplifiers,” *IEEE Transactions on Signal Processing*, vol. 54, no. 10, pp. 3852–3860, 2006.

